Volume 15 | Number 23 | 7 December 2015 | Pages 4371–4490

Lab on a Chip

Miniaturisation for chemistry, physics, biology, materials science and bioengineering

www.rsc.org/loc

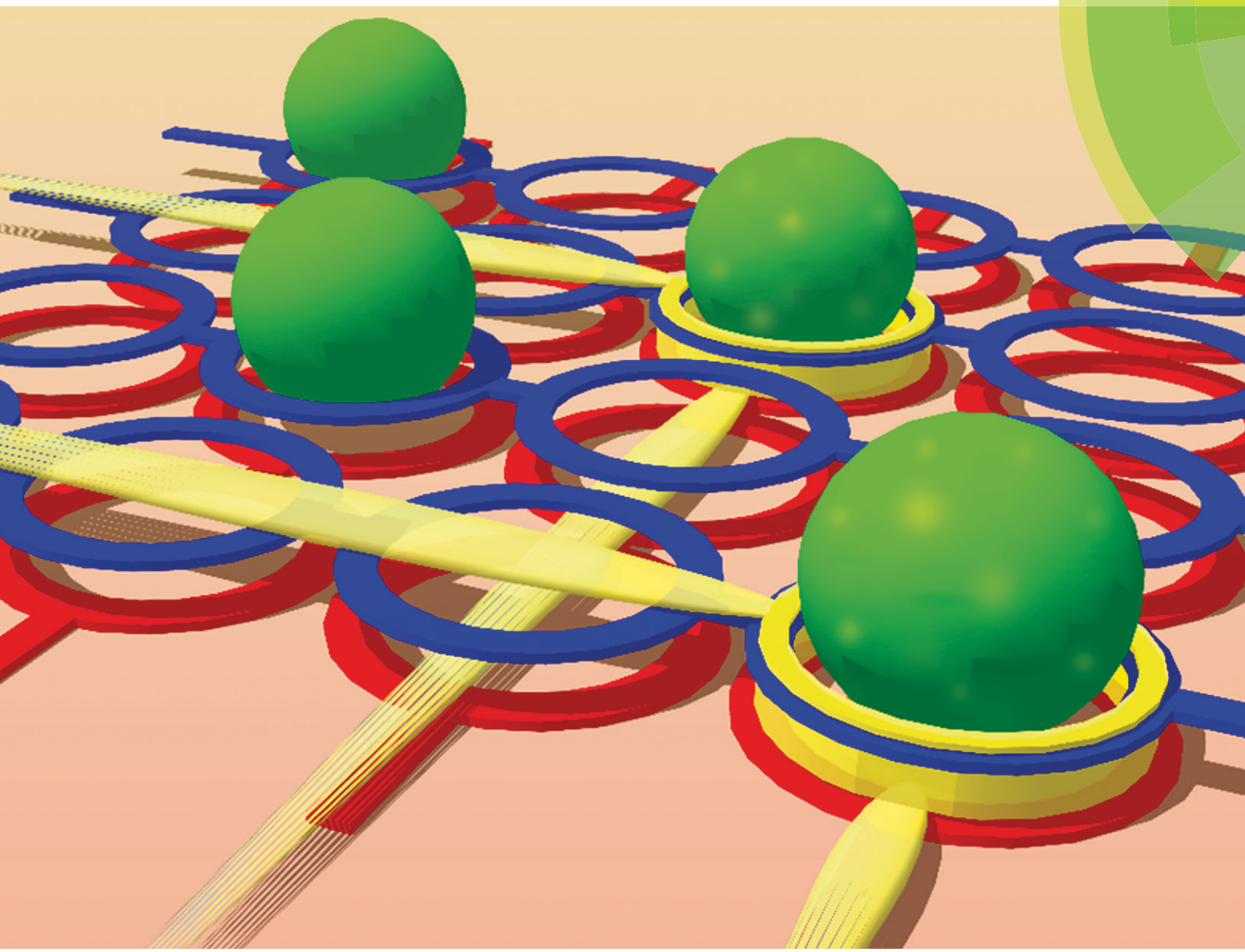

ISSN 1473-0197

ROYAL SOCIETY OF CHEMISTRY

PAPER

Kosuke Ino, Tomokazu Matsue *et al.*

A local redox cycling-based electrochemical chip device with nanocavities for multi-electrochemical evaluation of embryoid bodies

Lab on a Chip

PAPER

View Article Online
View Journal | View Issue

Cite this: *Lab Chip*, 2015, **15**, 4404

A local redox cycling-based electrochemical chip device with nanocavities for multi-electrochemical evaluation of embryoid bodies†

Yusuke Kanno,[a] Kosuke Ino,*[a] Hitoshi Shiku[a] and Tomokazu Matsue*[ab]

Received 25th August 2015,
Accepted 6th October 2015

DOI: 10.1039/c5lc01016k

www.rsc.org/loc

An electrochemical device, which consists of electrode arrays, nanocavities, and microwells, was developed for multi-electrochemical detection with high sensitivity. A local redox cycling-based electrochemical (LRC-EC) system was used for multi-electrochemical detection and signal amplification. The LRC-EC system consists of n^2 sensors with only $2n$ bonding pads for external connection. The nanocavities fabricated in the sensor microwells enable significant improvement of the signal amplification compared with the previous devices we have developed. The present device was successfully applied for evaluation of embryoid bodies (EBs) from embryonic stem (ES) cells *via* electrochemical measurements of alkaline phosphatase (ALP) activity in the EBs. In addition, the EBs were successfully trapped in the sensor microwells of the device using dielectrophoresis (DEP) manipulation, which led to high-throughput cell analysis. This device is considered to be useful for multi-electrochemical detection and imaging for bioassays including cell analysis.

Introduction

Electrochemical methods have been applied to bio/chemical assay devices because they afford a sensitive, miniaturized, and easy-to-handle detection scheme, which is particularly required in sophisticated devices with high sensitivity and high throughput that are fabricated using micro/nanofabrication techniques. For example, micro/nanofluidic devices have been developed for electrochemical detection, where microfluidic chips with a band-electrode detector were used for faster and simpler on-site monitoring of chemical species in a capillary electrophoresis electrochemical (CE-EC) system.[1] Microfluidic chip devices also enable manipulation of biomaterials such as live cells, such that microfluidic electrochemical devices have also been applied for high-throughput cell analysis and as cell-based biosensors.[2,3] For a highly sensitive electrochemical assay, several methods have been developed. For example, the sensitivity of electrochemical detection can be significantly improved using a redox cycling system[4–20] in which two sets of electrodes are located in close proximity to one another. A redox species generated at one electrode diffuses to the other electrode where an electrochemical reaction regenerates the original species. Redox cycling between the two electrodes amplifies the electrochemical response.[4,5] The amplification factor increases with a decrease in the distance between the electrodes; that is why nanofabrication processes for nanofluidic/nanocavity electrochemical devices with redox cycling detection have received much attention. Nanocavities have been fabricated by layer-by-layer metal assembly with a thin sacrificial Cr layer, followed by the sacrificial etching of the Cr layer to prepare nanocavities between the metal layers such as Au electrodes.[6] Application of appropriate potentials to these electrodes leads to the reaction of the target molecules, such as catechol,[6] in these electrodes and the redox cycling between the nanocavities is induced, which provides an amplified electrochemical current. Rassaei and coworkers reported that quinone as an enzymatic reaction product is localized in the confined space of a nanochannel in which efficient redox cycling also occurs, so that the sensor allows sensitive detection of the product molecules generated by the enzyme in real time.[8] Excellent sensitivity can be achieved, which Lemay and coworkers have reported in the detection of single molecules using nanocavity devices.[9,12,17]

In addition, micro/nanofabrication techniques have been applied for the integration of many sensors into a single chip device to realize electrochemical multi-detection and imaging. Chip devices that consist of microelectrodes have also been used for electrochemical cell analysis.[21–23] However, it is difficult to prepare many sensors on a small chip due to the lack of space for lead connections and connector pads. Thus, we have previously reported a redox cycling-based

[a] *Graduate School of Environmental Studies, Tohoku University, Japan. E-mail: ino.kosuke@bioinfo.che.tohoku.ac.jp, matsue@bioinfo.che.tohoku.ac.jp*
[b] *WPI-Advanced Institute for Materials Research, Tohoku University, Japan*

† Electronic supplementary information (ESI) available. See DOI: 10.1039/c5lc01016k

electrochemical system to incorporate many sensors within a small space.[24–31] The system consists of n column and n row electrodes to form n^2 crossing points with $2n$ bonding pads for external connection. The application of appropriate potentials to these electrodes induces redox cycling only at the desired crossing points, which allows the crossing points to be used as individual sensors. We have designated this novel methodology as local redox cycling-based electrochemical (LRC-EC) detection. Thus, n^2 sensors can be easily incorporated into a small chip device with only $2n$ bonding pads for external connection. In our previous studies, comb-type interdigitated array (IDA) electrodes were incorporated at each sensor point of the device[24–26] to detect the electrochemical signal induced by the redox cycling.[32] Cell differentiation of embryonic stem (ES) cells *via* their alkaline phosphatase (ALP) activity, which is known as an undifferentiation marker of ES cells, was successfully imaged using the LRC-EC device with IDA electrodes that had a typical 5 μm gap between the electrode fingers.[24] The sensitivity can be improved using short-gap IDAs; however, fabrication of an IDA with nanometer size gaps is technically difficult. Therefore, nanocavity electrodes have been incorporated into the LRC-EC system to increase the redox cycling efficiency and thereby improve the signal amplification.

In the present study, nanocavities were fabricated in the LRC-EC devices for highly sensitive electrochemical detection. The gap between the sensor electrodes for the redox cycling was 230 nm, which is considerably smaller than the 5 μm gaps in our previous device.[24] In addition, microwells were incorporated into the device to trap the embryoid bodies (EBs) of the ES cells for stable analysis. The ALP activities of the trapped EBs were evaluated using the device based on the redox cycling in the nanocavities. In addition, dielectrophoresis (DEP) manipulation was applied to trap the EBs in the microwells.

Materials and methods

Detection system

The general architecture of the device and setup is displayed in Fig. 1A. The LRC-EC device consisted of 4 row and 4 column electrodes. The top and bottom ring electrodes were connected to the row and column electrodes, respectively, and these ring electrodes were placed at the individual crossing points of the row and bottom electrodes. The top and bottom ring electrodes were separated with nanocavities (230 nm high). A multichannel potentiostat (HA-1010 mM4, Hokuto Denko, Japan) was connected to these electrodes through a clip connector (CCNL-050-37-FRC, Yokowo, Japan) and a switching matrix (NI PXI-2529, National Instruments, USA). Voltage control and data collection were performed using a program written with LabVIEW (National Instruments). SU-8 microwell arrays were fabricated at the individual crossing points. Local redox cycling was induced only at

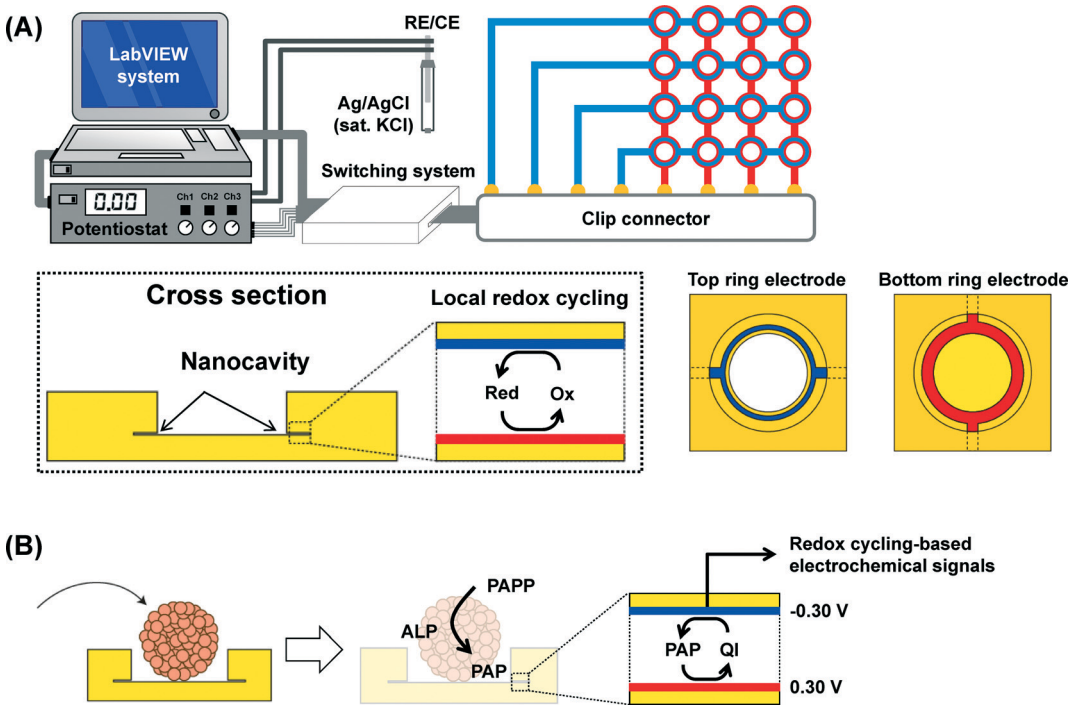

Fig. 1 General outline of the LRC-EC device with nanocavities and microwells. (A) Illustration of the detection system. The device consists of 4 row electrodes containing the top ring electrodes (blue) and 4 column electrodes containing the bottom ring electrodes (red). These ring electrodes are placed at the individual crossing points. The microwell arrays are fabricated at the individual crossing points, and the top and bottom ring electrodes are separated by nanocavities (230 nm high). Redox cycling is locally induced at the designated crossing points. (B) Detection scheme for the ALP activity in the EBs. The EBs are trapped in microwells filled with PAPP and the enzymatic product by ALP, PAP, is measured. Electrochemical signals for the redox cycling of PAP/QI are acquired.

the ring electrodes located at the designated cross points. A sample solution was introduced onto the sensor area, and an Ag/AgCl (sat. KCl) electrode as a reference and a counter electrode was inserted into the solution.

The EBs were introduced into a solution on the device to trap a single EB in a microwell (Fig. 1B). *p*-Aminophenyl phosphate (PAPP) in a solution was catalytically hydrolyzed by alkaline phosphatase (ALP) on the EBs to yield *p*-aminophenol (PAP) which can then be detected using redox cycling (Fig. 1B).[24] The redox cycling of PAP and the oxidation product, *p*-quinone imine (QI), was measured by the device. For imaging, the electrochemical responses at the 16 sensor microwells were collected by sequentially changing the potential applied to the row and column electrodes.

Device fabrication

The device fabrication process is described in Fig. 2. The nanocavities were fabricated by etching of sacrificial Cr layers, according to previous studies.[7–11,13,14,17–19] Briefly, Ti/Pt was sputtered onto a glass substrate (Matsunami Glass Ind., Ltd., Japan) to fabricate the bottom ring electrodes (outer diameter: 195 μm, inner diameter: 150 μm) connected to the column electrodes. The bottom ring electrodes were used as the generator electrodes.[33] Cr was sputtered onto the column electrodes to prepare the sacrificial Cr layer. Cr/Pt was then sputtered to fabricate the top ring electrodes connected to the row electrodes. The top ring electrodes were used as the collector electrodes.[33] The configuration of the metal layers was observed using a 3D laser scanning confocal microscope (VK-X200, Keyence, Japan). A SU-8 layer (50 μm thick, SU-8 3050, Microchem Co., USA) was fabricated on the device to form 4 × 4 microwells (diameter: 150 μm, depth: 50 μm, center-to-center distance: 300 μm). The sacrificial Cr layers were then etched with a Cr etching solution (3% perchloric acid solution containing 0.12 M ammonium hexanitratocerate(IV)) to prepare nanocavities between the top and bottom ring electrodes. During the etching process, the column and row electrodes were connected with a digital voltmeter (Custom Corp. CDM-2000D, Japan), and the resistance between these electrodes was monitored to evaluate the etching process (Fig. S1†).

Redox current simulation

Redox currents from the top and bottom ring electrodes were calculated using COMSOL Multiphysics (version 5.1, COMSOL, Inc., USA).[24,34,35] A three-dimensional model containing the nanocavities, ring electrodes and microwells is described in Fig. S2 and S3.† To simplify the calculation, the lead electrodes were removed and the simple ring electrodes were arranged (Fig. S2 and S3†). Ferrocenemethanol ($FcCH_2OH$) was used as the redox compound. For the detection of $FcCH_2OH$, the electrochemical system is assumed to be a reversible one-electron reaction in the simulation. The initial concentration of $FcCH_2OH$ is set at 1.0 mM.[36] The diffusion coefficients of $FcCH_2OH$ and $FcCH_2OH^+$ are set at 7.0×10^{-10} m^2 s^{-1}, which indicates that the sum of

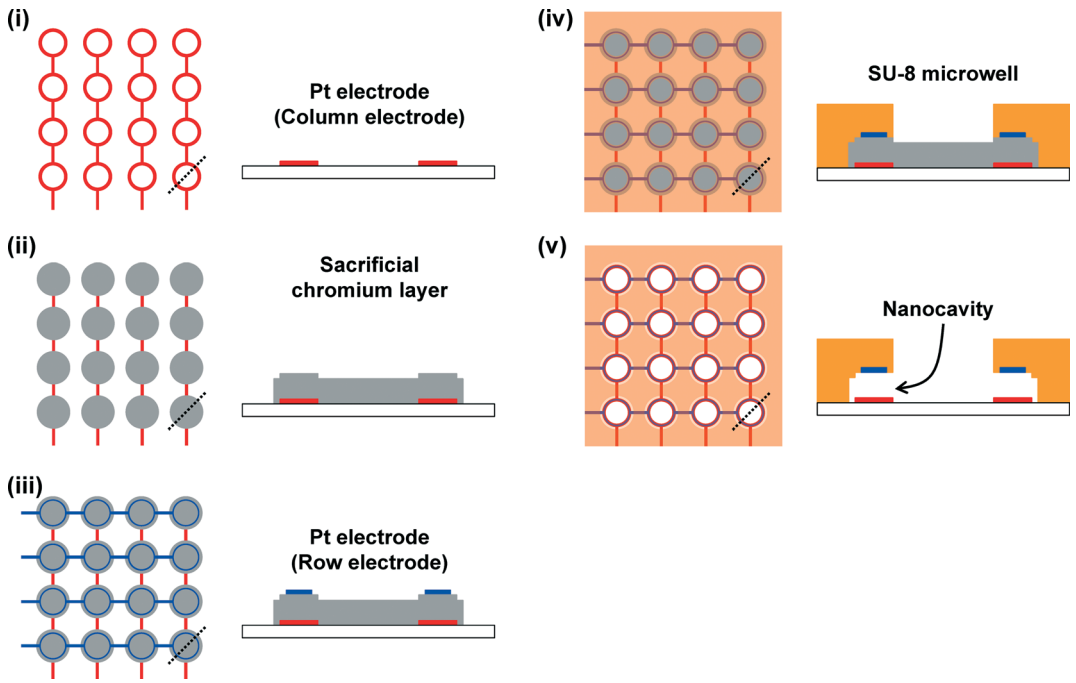

Fig. 2 Schematic illustration of the device fabrication process. (i) Ti/Pt is sputtered onto a glass substrate to fabricate the column electrodes that contain the bottom ring electrodes. (ii) A sacrificial Cr layer is sputtered on the bottom ring electrodes. (iii) Cr/Pt is then sputtered to fabricate the row electrodes that contain the top ring electrodes. (iv) A SU-8 layer is fabricated on the device to form 4 × 4 microwells (diameter: 150 μm, depth: 50 μm, gap: 300 μm). (v) The Cr sacrificial layer is etched to prepare nanocavities between the top and bottom ring electrodes.

$FcCH_2OH$ and $FcCH_2OH^+$ is equal to the initial concentration of $FcCH_2OH$ in the space during electrochemical detection. The concentrations of $FcCH_2OH$ and $FcCH_2OH^+$ at the electrodes during the electrochemical reaction are calculated using the Nernst equation. The standard electrode potential of the redox compound is set to 0.216 V.[37]

For cyclic voltammetry in the redox cycling mode, the bottom electrode (generator) was scanned from 0.00 to 0.50 V at 100 mV s^{-1}, while the top electrode was held at 0.00 V. The collection efficiency was defined as the ratio of the cathodic currents at the collector electrodes to the anodic currents at the generator electrodes when the potential of the generator electrodes reached 0.50 V. For amperometry in the redox cycling mode, a bottom electrode (generator) was stepped to 0.50 V, while a top electrode was held at 0.00 V. The currents at 10 s were used for the calculation of the signal amplification. The responses were acquired from these electrodes when the channel heights were changed from 230 nm to 30 μm. For amperometry in the non-redox cycling mode, a ring electrode was prepared on the bottom of the microwell (Fig. S3†), and the potential was stepped to 0.50 V. The currents at 100 s were then used for the calculation of the signal amplification.

Characterization of the device

The electrochemical performance of the LRC-EC device with nanocavities was investigated using $FcCH_2OH$. Sample solutions were introduced by pipetting after O_2 plasma ashing of the device. The column electrode was stepped from 0.00 to 0.50 V, while the other electrodes were held at 0.00 V. The connection of these electrodes is shown in Fig. S4.† Redox cycling-based responses from $FcCH_2OH$ in a Tris-HCl buffer (pH 9.5) at the row electrodes were acquired to prepare a calibration curve for $FcCH_2OH$ from a single sensor.

Cell culture

Mouse ES cells (129/Sv) were cultured according to a previous report.[24] Briefly, the ES cells were cultured in Stem Medium (Dainippon Sumitomo Pharma, Japan) supplemented with 1 mM mouse leukemia inhibitory factor (mLIF) and 0.1 mM 2-mercaptoethanol, and the culture medium was changed every day. The EBs were formed by the hanging drop method.[38] The ES cells were suspended in Stem Medium supplemented with 15% fetal bovine serum (FBS) and no mLIF. The suspension was introduced onto the cover of a culture dish to form 20 μL droplets containing 500 cells. The droplets were then hung from the dish cover and the culture dish was incubated for 1 day to form the EBs. The EBs were introduced into the device using a capillary.

Electrochemical detection of ALP activity in the EBs

A Tris-HCl solution (pH 9.5) containing 4.0 mM PAPP (LKT Laboratories, USA) and 2 mM $MgCl_2$ was introduced into the device and the EBs were then introduced into the microwells on the device using a capillary under a microscope. For the activation of ALP, $MgCl_2$ was added. The detection scheme based on the redox cycling for ALP detection is shown in Fig. 1B. PAPP is catalytically hydrolyzed by ALP on the EBs to yield PAP. PAP is oxidized at the bottom ring electrodes (generator, 0.30 V) and the oxidation product, QI, diffuses to the top ring electrodes (collector, −0.30 V). QI is then reduced back to PAP at the top ring electrodes (collector, −0.30 V) and diffuses back to the bottom ring electrodes to be reoxidized. The redox cycling between the top and bottom ring electrodes amplifies the electrochemical signal from PAP produced by ALP on the EBs. Fig. S5† shows an imaging process for the detection of the ALP activity in the EBs. Briefly, redox-cycling based electrochemical signals were sequentially acquired by application of appropriate potentials to these electrodes to complete detection at all sensors. Electrochemical detection was performed in a Faraday cage.

DEP for the manipulation of the EBs using the LRC-EC device with nanocavities

For the DEP manipulation, an indium tin oxide (ITO) electrode was mounted face-to-face onto the device with a 260 μm thick spacer. The ITO electrode and the ring electrodes in the device were connected to a function generator (Hioki E. E. Co., Nagano, Japan). EBs in a 0.2 M sucrose solution were introduced into the 260 μm high interspace between the ITO substrate and the device. Alternating electric fields (10 MHz, 20 V_{pp}) of opposite phases were then applied to the ring electrodes and the ITO electrode, respectively. After the manipulation of the EBs using DEP, the 0.2 M sucrose solution was flushed in the interspace to remove the excess EBs.

Results and discussion

Current simulation

A cyclic voltammetry simulation for the redox compounds was conducted to clarify the signal amplification, collection efficiency, crosstalk, and time to reach steady-state. The configuration of the electrodes used for the simulation is shown in Fig. 3A and S2.† When the cavity height is set at 20 μm, the collector current from the top electrode and the generator current from the bottom electrode at 0.50 V were −37.2 and 46.6 nA, respectively, and the collection efficiency was 80% (Fig. 3B). However, for a nanocavity height of 230 nm, the collector current from the top electrode and the generator current from the bottom electrode were −1.47 and 1.48 μA, respectively, and the collection efficiency was approximately 100% (Fig. 3B). These results indicate that there is no crosstalk because the diffusion layer does not broaden during electrochemical detection when using a 230 nm gap. Fig. 3C shows that the collector signals are inversely proportional to the nanocavity height. Thus, the collector currents are strictly dependent on the distance between the top and the bottom electrodes. The collection efficiency increases with a decrease in the distance and reaches approximately 100% when the nanocavity height is 230 nm (Fig. 3D).

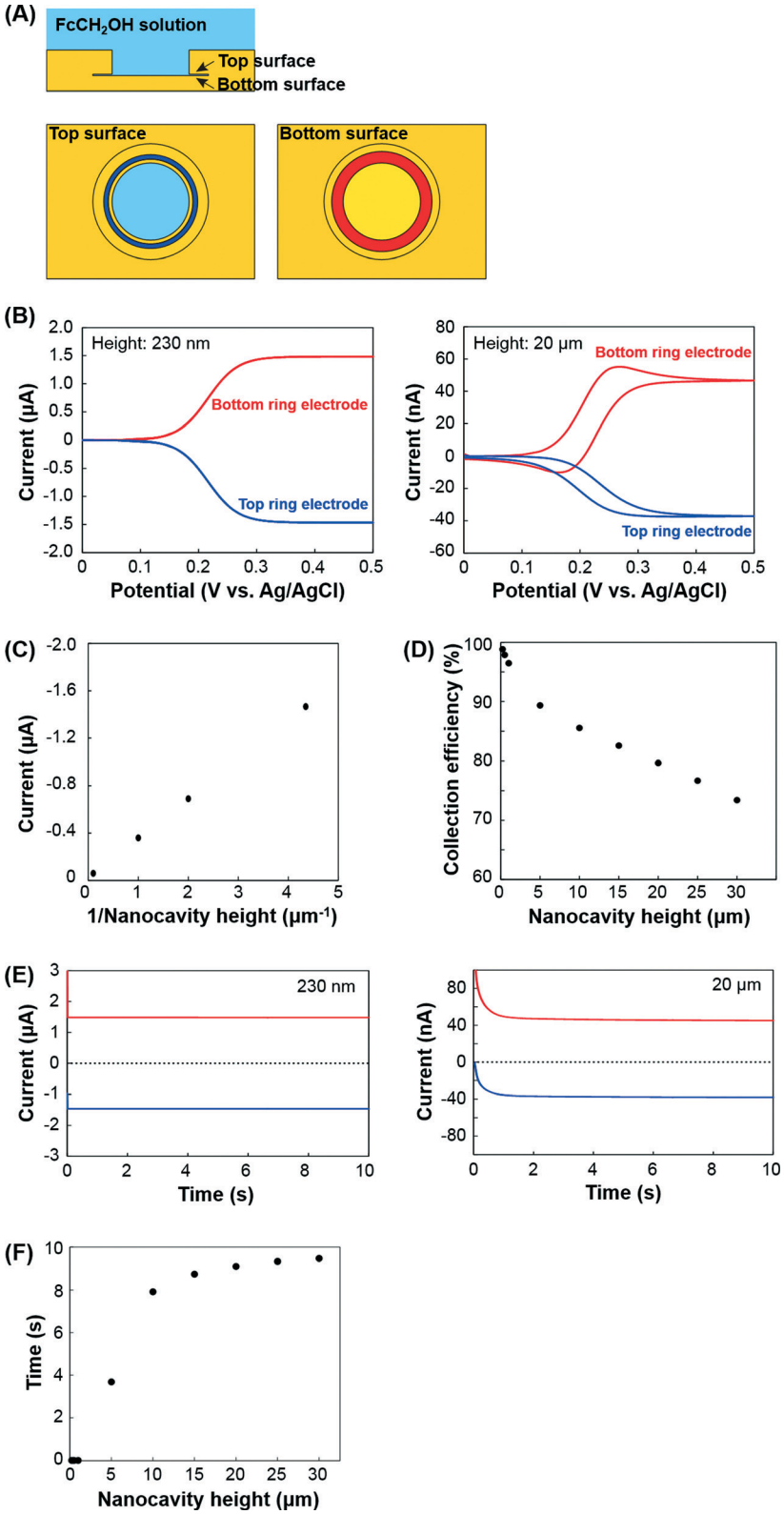

Fig. 3 Cyclic voltammograms and chronoamperograms obtained for the top and bottom ring electrodes using the simulation software. (A) Illustration of the simulation model consisting of the top and bottom electrodes. The top and bottom electrodes are used as the collector and generator electrodes, respectively. The detailed configuration is shown in Fig. S2.† The nanocavity heights ranged from 230 nm to 30 μm. The nanocavity is filled with 1.0 mM $FcCH_2OH$ solution. (B) Cyclic voltammograms for the nanocavity heights of 230 nm and 20 μm. The potential of the bottom ring electrode was scanned from 0.00 to 0.50 V at 100 mV s^{-1} while the potential of the top ring electrode was kept at 0.00 V. (C) Currents in the cyclic voltammograms measured at 0.50 V. (D) Collection efficiency in the cyclic voltammograms measured at 0.50 V. (E) Chronoamperograms for the nanocavity heights of 230 nm and 20 μm. The potential of the bottom ring electrode was stepped to 0.50 V while the potential of the top ring electrode was maintained at 0.00 V. (F) Time to reach the steady-state current (99.9% of the reduction currents at 10 s) for the nanocavity heights from 230 nm to 30 μm.

Fig. 3E and F show the results for the amperometric simulation. The time to reach steady-state was significantly dependent on the channel height. With the nanocavities, the time to reach the steady-state can be significantly shortened because a steady-state diffusion layer forms in the cavity within a short period. Therefore, the LRC-EC device with nanocavities can be applied for rapid electrochemical imaging.

When both the top and bottom electrodes are synchronously stepped to 0.50 V (non-redox cycling mode), the redox compounds are consumed by the top and the bottom electrodes, which causes depletion of the redox compounds in the cavity. As a result, the current decreases to background current. Therefore, the electrochemical current from a simple ring electrode was calculated and used as a reference value in the non-redox cycling mode to evaluate the signal amplification of redox cycling in the device. The configuration of the simple ring electrodes is given in Fig. S3.† From the amperometric simulation of the non-redox cycling condition, the current was approximately 15 nA at 100 s (Fig. S3†). In contrast, the current in the redox cycling mode was approximately −1.5 μA when using a 230 nm gap (Fig. 3E), which is almost 100 times larger than that in the non-redox cycling mode. Thus, the system with nanocavities is useful for highly sensitive and rapid electrochemical assay.

Device fabrication

Fig. 4 shows the process for the device fabrication. The layer thicknesses of the present device were as follows: the first Ti/Pt layer, 70 nm (Fig. 4A); the second Cr layer, approximately 200 nm (Fig. 4B); and the third Cr/Pt layer, 130 nm (Fig. 4C). The total thickness of the sacrificial Cr between the top Pt and bottom Pt electrodes was 230 nm.

Fig. 5A and Movie S1† show optical images during the etching process of the sacrificial Cr layer. After adding the Cr etching solution into the microwells, the sacrificial Cr layer was removed gradually. After etching for approximately 25 min, the resistance between the top and bottom electrodes increased sharply (Fig. 5B), which indicates complete removal of the Cr sacrificial layer between the ring electrodes. The percentage of functional structures fabricated with the etching process was 50%, and the rest of the devices showed a short circuit. In addition, 30% of the functional devices were suitable for redox cycling-based detection.

A silicon layer is also utilized for a sacrificial layer for nanofluidics.[20,39] To remove the silicon sacrificial layer, reactive ion etching using SF_6 gas or etching solutions with high temperature are used. In contrast, we utilized a sacrificial chromium layer because the etching process is easily performed and allows high selectivity and a well-controlled etch rate. Materials for sensing electrodes should show proper adherence to chromium for layer-by-layer fabrication, which is the limitation when deciding the materials of the electrodes. Since Pt and Au meet the limitation, Pt was chosen in the present study.

Fig. 6 shows the optical images of the LRC-EC device with nanocavities. The device consisted of 16 electrochemical

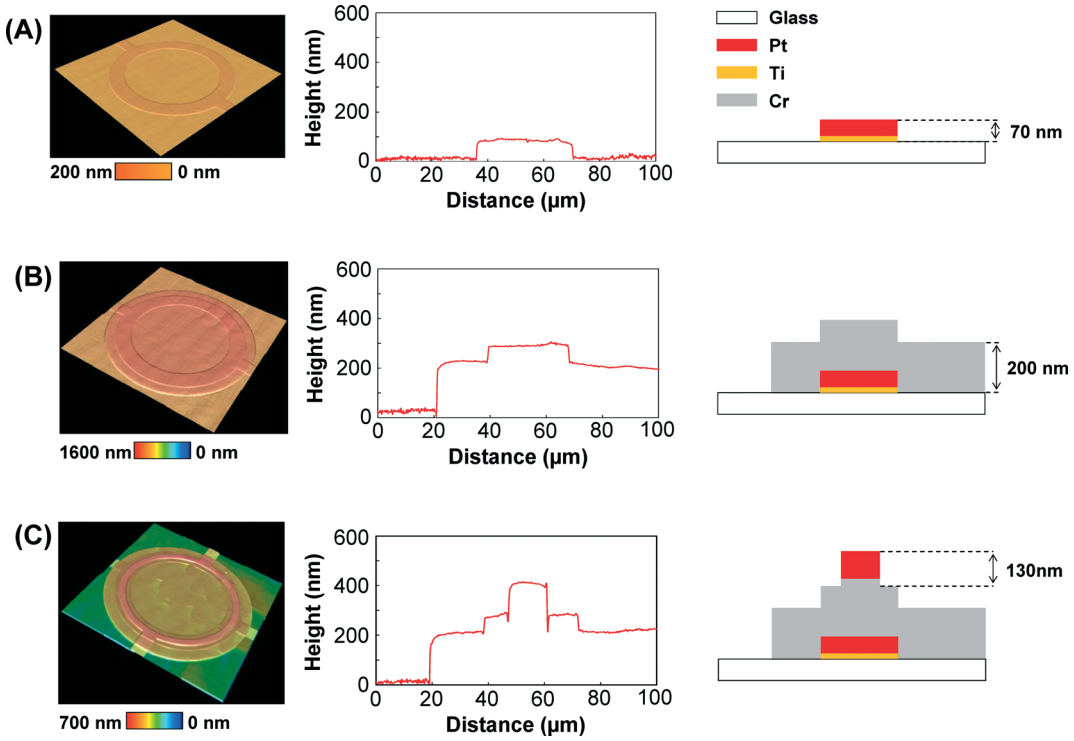

Fig. 4 Configuration of the metal layers in each fabrication process. Three-dimensional (3D) topographies of (A) the first layer of Ti/Pt, (B) the second layer of Cr, and (C) the third layer of Cr/Pt. Heights of the metal layers and cross-sectional illustrations.

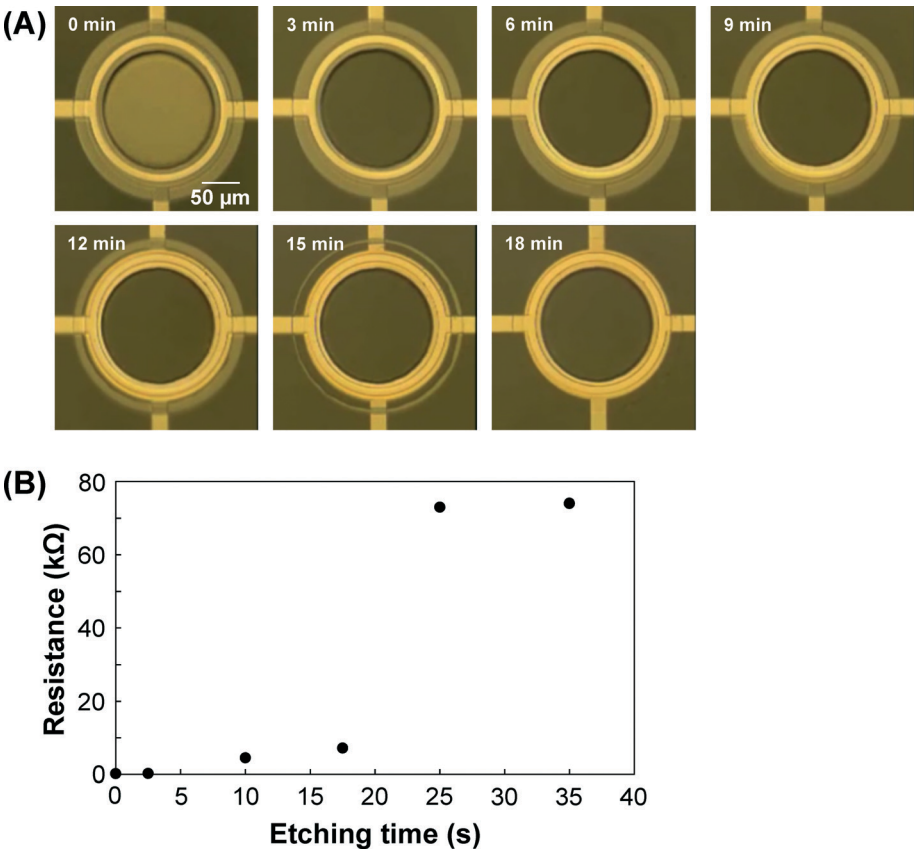

Fig. 5 Time-course images of the device during etching of the sacrificial Cr layer. (A) Optical images. (B) Time-course analysis for the resistance between the top and bottom electrodes during the etching process. The movie for this process is shown in Movie S1.†

sensors and only 8 connector pads. The top and bottom ring electrodes were prepared at the crossing points, which were separated by the 230 nm high nanocavities. The center-to-center distance of the sensors was 300 μm. Microwells that are 150 μm in diameter and 50 μm in depth were prepared at the crossing points to trap the EBs.

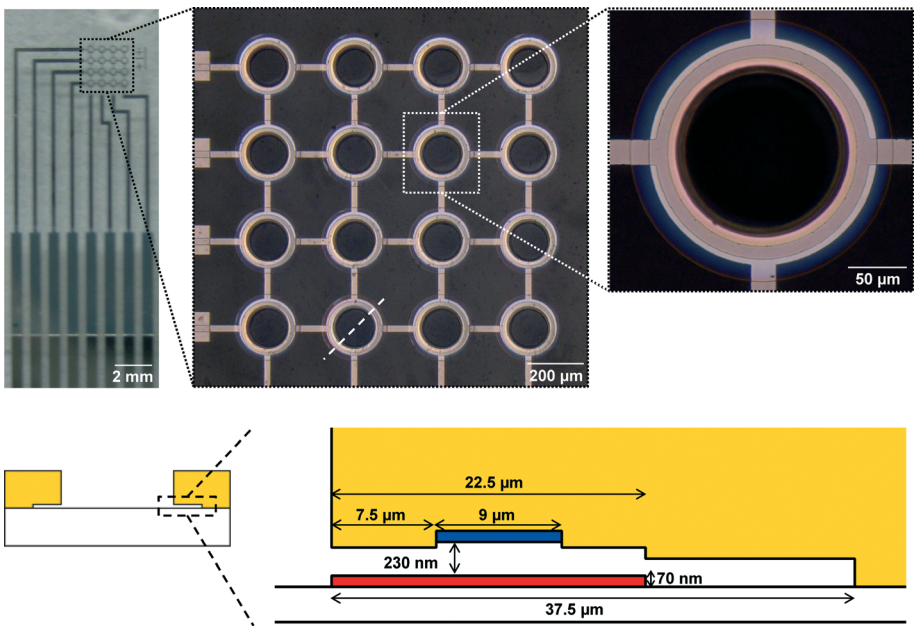

Fig. 6 Optical images of the LRC-EC device with nanocavities and microwells, and cross-sectional diagrams of the device.

The fabrication process for the device with nanocavity is slightly complex, compared to our previous devices,[24–31] which is its disadvantage.

Calibration curve

Chronoamperometry using the device demonstrated that redox cycling was rapidly established so that steady-state currents could be rapidly acquired (Fig. 7A). The electrochemical signals at the sensors were proportional to the concentration of $FcCH_2OH$ (Fig. 7B) and the detection limit of $FcCH_2OH$ was less than 100 nM; therefore, the device can be used for the quantitative detection of redox components in the nanocavities. According to the calibration curve, the electrochemical signal for 1.0 mM $FcCH_2OH$ was estimated to be approximately −1.0 μA, which was approximately two-thirds of the simulation current (−1.5 μA). This discrepancy may be caused by fouling of the electrodes and/or deformation of the channels.

According to our previous work using interdigitated ring array (IDRA) electrodes with a 5 μm gap, the current density of a collector electrode was estimated to be approximately 0.16 pA μm^{-2} for 10 μM $FcCH_2OH$.[30] On the other hand, the current density was approximately 1.9 pA μm^{-2} (Fig. 7), which was 12 times higher than that of the previous device due to highly effective redox cycling in the nanocavity. Therefore, the device with the nanocavity was more sensitive than the previous device.

Electrochemical imaging of the ALP activity in the EBs

Fig. 8 shows an electrochemical image of the ALP activity in the EBs (*ca.* 150 μm in diameter). The electrochemical images follow the position of the EBs (Fig. 8B and C). When no PAPP was added to the solution, no electrochemical signals were acquired from the sensors with the EBs. These results clearly demonstrate that the electrochemical signals were derived from the redox cycling of PAP/QI after catalytic hydrolysis of PAPP by ALP (Fig. 8D). PAPP was chosen because it is a common substrate for the redox cycling-based detection of ALP and it is commercially available. Other substrates for the electrochemical detection of ALP are described in the ESI.†

We have previously reported that electrochemical methods can be applied for the evaluation of ES cell differentiation *via* their ALP activity.[40] The LRC-EC system is especially useful for multi-electrochemical detection of ES cell differentiation.[24,26,29–31] Furthermore, the present LRC-EC system is superior to our previous devices in terms of the sensitivity due to the efficient redox cycling in the nanocavities. In our previous paper,[29] IDRA electrodes with a 5 μm gap were successfully applied for detection of EB differentiation. The current density of a collector electrode was approximately 1.9 pA μm^{-2} from each EB that was fabricated by 1 day culture of 500 cells in a 20 μL droplet. In the present study, the current density was approximately 39 pA μm^{-2}, which was 21 times higher than that of the previous study. Therefore, the present device was more sensitive than the previous devices due to the highly effective redox cycling in the nanocavity.

According to the calibration curve (Fig. 7B) and the electrochemical image (Fig. 8), the PAP concentration on the sensors was estimated to be approximately 100 μM, considering that the electrochemical systems are one- and two-electron reactions for $FcCH_2OH$ and PAP, respectively. The estimated value is smaller than that in our previous studies (approximately 200–300 μM),[24] because the EBs were slightly further away from the sensors in the present study.

Although a high pH will affect EB differentiation, a high pH solution was used for the ALP detection because the pH is suitable for ALP activity compared to neutral pH. We have reported the electrochemical detection of ALP in neutral pH, and the electrochemical signals became 1/5–1/10.[24,29] Since the electrochemical signals were sufficiently acquired in the present method, a neutral pH solution can be used for detection. Detection in the neutral pH can provide no significant influence on cell viability and cell differentiation.

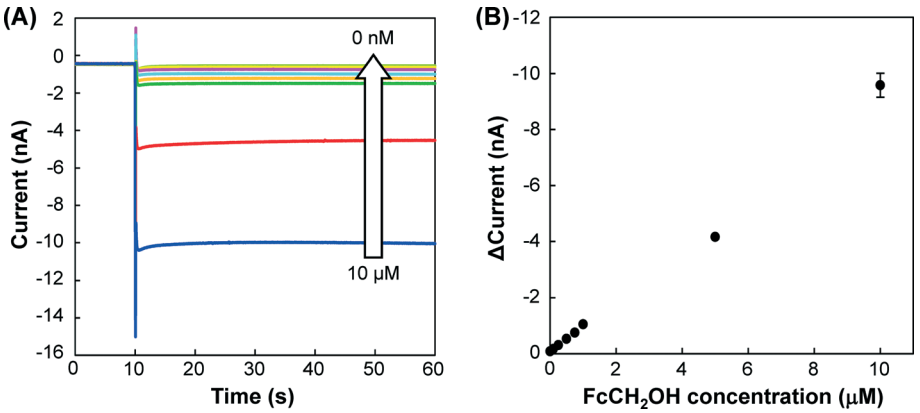

Fig. 7 Dependence of the electrochemical signals on the $FcCH_2OH$ concentration. (A) Chronoamperograms at the row electrodes where the potential was maintained at 0.00 V while the column electrodes were stepped from 0.00 to 0.50 V. The connections of these electrodes are shown in Fig. S4.† (B) Calibration curve. The currents were obtained from the row electrodes. The currents at 60 s were subtracted from those at 9.96 s for the background-corrected currents, and these values were plotted on a graph (N = 3).

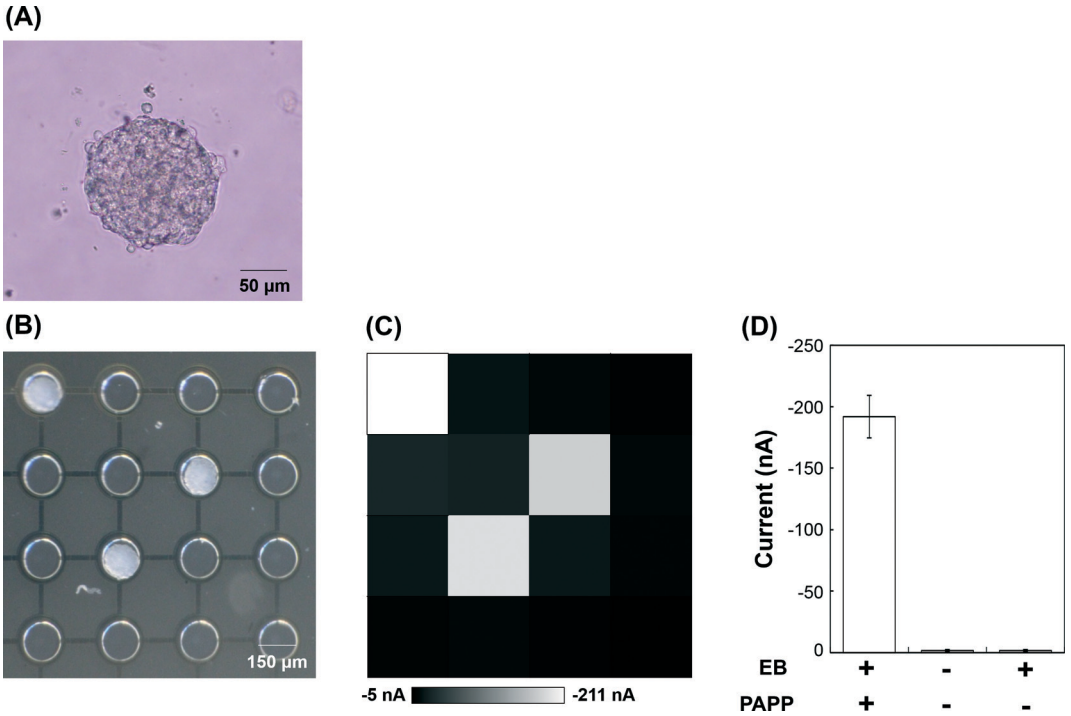

Fig. 8 Electrochemical imaging of the ALP activity in the EBs. (A) Hanging droplets (500 cells, 20 μL) were incubated for 1 day to prepare EBs that are approximately 150 μm in diameter. (B) Optical image of the EBs on the device. (C) Electrochemical image of the ALP activity in the EBs. The electrochemical signals were derived from the redox cycling-based reaction of PAP, which is the enzymatic product of ALP reaction in the EBs. (D) The currents were plotted on a graph (N = 3).

Since the detection limit of $FcCH_2OH$ was less than 100 nM, the detection limit of PAP is estimated to be less than 50 nM according to the number of transferred electrons in the reaction of $FcCH_2OH$ and PAP. Although single ALP molecules on the EBs cannot be detected since the ALP of the EBs is not secreted ALP, there is some possibility of detecting the single ALP molecules if ALP is introduced into the nanocavity.

The LRC-EC device can also be applied for the detection of neurotransmitters, such as dopamine, from dopaminergic cells. Dopamine is a key species for the treatment of Parkinson's disease;[41] therefore, highly sensitive detection of dopamine and related compounds will attract attention for cell-based therapy using dopaminergic cells.

DEP for the manipulation of the EBs using the LRC-EC device with nanocavities

DEP was reported by Pohl as the motion of dielectric particles under a non-uniform electric field.[42] DEP can be used to manipulate various particles, including non-charged particles, such that DEP techniques have been applied to separate, concentrate, or align target particles.[43–51] In the present study, the device was used to induce positive DEP (pDEP) for the preparation of the EB arrays. Under pDEP, the particles are moved to the direction of a strong electric field. Fig. 9A shows the scheme for the manipulation of the EBs using pDEP as the driving force. An AC electric field was applied between the ring electrodes in the device and the ITO substrate placed above the device. A non-uniform electric field was formed at the open space of the microwell, and the resulting pDEP force guided an EB into the microwell with the ring electrode and nanocavity (Fig. 9B and Movie S2†). Only single EBs were trapped in the microwells because the size of the microwell was matched to the size of a single EB (Fig. 9B). The excess EBs were flushed away by introducing sucrose solution into the space. When the flushed EBs passed above empty microwells, they became trapped in the microwells due to DEP (Fig. 9B and Movie S2†). The DEP effect was sufficiently strong to hold the EBs in the microwells under solution flow. Thus, a single EB array was easily fabricated using the DEP technique, which demonstrates that the electrochemical system is useful for cell analysis.

We have previously reported that pDEP in a 0.2 M sucrose solution did not affect cell viability of HeLa cells.[52] Therefore, we assumed that a 0.2 M sucrose solution did not affect the cell viability of the ES cells. However, the previous paper showed that the DEP manipulation is not completely stress free, indicating that the DEP might affect cell differentiation of the ES cells. Another study reported that cells are damaged at an electric field strength above 1 kV cm^{-1}.[53] We simulated the electric field strength on the device under DEP and confirmed that it is below 1 kV cm^{-1} around an EB (Fig. S6†). These results also indicated that the DEP manipulation did not affect cell viability. The detailed influence of DEP on cell viability and cell differentiation is under investigation.

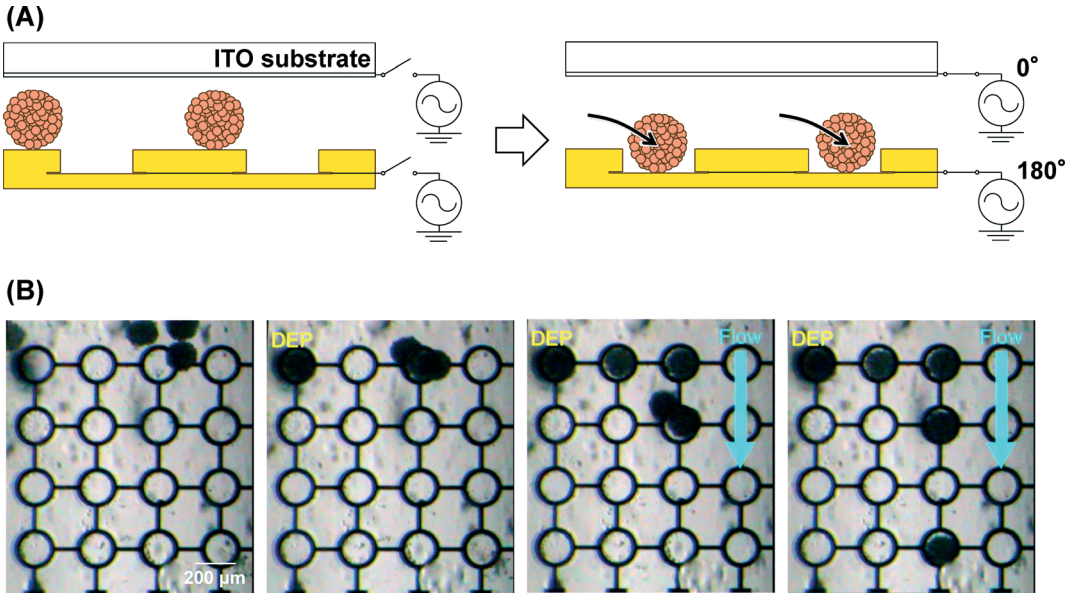

Fig. 9 Manipulation of the EBs using DEP. (A) Scheme for the capture of the EBs using DEP. (B) Optical images of the EBs on the device during DEP manipulation and fluidic manipulation. The movie for this process is shown in Movie S2.†

Wolfrum and colleagues reported nanocavities incorporated into an LRC-EC system,[19] and addressable detection was performed. In the present study, we have demonstrated that the LRC-EC device with nanocavities and microwells can be applied for the evaluation and manipulation of EBs, which suggest that the present system is useful for cell analysis.

Conclusion

An LRC-EC device with nanocavities and microwells was developed for multi-electrochemical detection with high sensitivity. The nanocavities enable significant improvement of the signal amplification compared to our previous research. The LRC-EC device with nanocavities was successfully applied for the evaluation of EBs *via* their ALP activity. In addition, the EBs were successfully trapped in the sensor microwells using DEP that was induced by the device, thereby enabling efficient cell analysis. The LRC-EC device thus demonstrated to be useful for bioassays including cell analysis.

Acknowledgements

This work was supported in part by a Grant-in-Aid for Scientific Research (A) (No. 25248032), a Grant-in-Aid for Young Scientists (A) (No. 15H05415) and a Grant-in-Aid for Challenging Exploratory Research (No. 26600057). This research was partly supported by the Special Coordination Funds for Promoting Science and Technology, Creation of Innovation Centers for Advanced Interdisciplinary Research Areas Program from the Japan Science and Technology Agency. This study was also supported by the Asahi Glass Foundation. This work was also supported by a Grant-in-Aid from Tohoku University Institute for International Advanced Research and Education.

References

1 J. Wang, *Talanta*, 2002, **56**, 223–231.
2 K. Ino, Y. Kitagawa, T. Watanabe, H. Shiku, M. Koide, T. Itayama, T. Yasukawa and T. Matsue, *Electrophoresis*, 2009, **30**, 3406–3412.
3 T. Yasukawa, K. Nagamine, Y. Horiguchi, H. Shiku, M. Koide, T. Itayama, F. Shiraishi and T. Matsue, *Anal. Chem.*, 2008, **80**, 3722–3727.
4 O. Niwa, M. Morita and H. Tabei, *J. Electroanal. Chem.*, 1989, **267**, 291–297.
5 K. Aoki, M. Morita, O. Niwa and H. Tabei, *J. Electroanal. Chem.*, 1988, **256**, 269–282.
6 B. Wolfrum, M. Zevenbergen and S. Lemay, *Anal. Chem.*, 2008, **80**, 972–977.
7 L. Rassaei, P. S. Singh and S. G. Lemay, *Anal. Chem.*, 2011, **83**, 3974–3980.
8 L. Rassaei, K. Mathwig, S. Kang, H. A. Heering and S. G. Lemay, *ACS Nano*, 2014, **8**, 8278–8284.
9 M. A. G. Zevenbergen, P. S. Singh, E. D. Goluch, B. L. Wolfrum and S. G. Lemay, *Nano Lett.*, 2011, **11**, 2881–2886.
10 E. Kaetelhoen, B. Hofmann, S. G. Lemay, M. A. G. Zevenbergen, A. Offenhaeusser and B. Wolfrum, *Anal. Chem.*, 2010, **82**, 8502–8509.
11 M. A. G. Zevenbergen, P. S. Singh, E. D. Goluch, B. L. Wolfrum and S. G. Lemay, *Anal. Chem.*, 2009, **81**, 8203–8212.
12 P. S. Singh, E. Kaetelhoen, K. Mathwig, B. Wolfrum and S. G. Lemay, *ACS Nano*, 2012, **6**, 9662–9671.
13 P. S. Singh, H.-S. M. Chan, S. Kang and S. G. Lemay, *J. Am. Chem. Soc.*, 2011, **133**, 18289–18295.
14 S. Kang, K. Mathwig and S. G. Lemay, *Lab Chip*, 2012, **12**, 1262–1267.
15 M. Hueske, R. Stockmann, A. Offenhaeusser and B. Wolfrum, *Nanoscale*, 2014, **6**, 589–598.

16 E. Kaetelhoen, K. J. Krause, P. S. Singh, S. G. Lemay and B. Wolfrum, *J. Am. Chem. Soc.*, 2013, **135**, 8874–8881.
17 S. Kang, A. F. Nieuwenhuis, K. Mathwig, D. Mampallil and S. G. Lemay, *ACS Nano*, 2013, **7**, 10931–10937.
18 D. Mampallil, K. Mathwig, S. Kang and S. G. Lemay, *Anal. Chem.*, 2013, **85**, 6053–6058.
19 E. Kaetelhoen, D. Mayer, M. Banzet, A. Offenhaeusser and B. Wolfrum, *Beilstein J. Nanotechnol.*, 2014, **5**, 1137–1143.
20 M. A. G. Zevenbergen, D. Krapf, M. R. Zuiddam and S. G. Lemay, *Nano Lett.*, 2007, **7**, 384–388.
21 L.-M. Li, W. Wang, S.-H. Zhang, S.-J. Chen, S.-S. Guo, O. Francais, J.-K. Cheng and W.-H. Huang, *Anal. Chem.*, 2011, **83**, 9524–9530.
22 K. Hayashi, T. Horiuchi, R. Kurita, K. Torimitsu and O. Niwa, *Biosens. Bioelectron.*, 2000, **15**, 523–529.
23 N. Kasai, C. X. Han and K. Torimitsu, *Sens. Actuators, B*, 2005, **108**, 746–750.
24 K. Ino, T. Nishijo, T. Arai, Y. Kanno, Y. Takahashi, H. Shiku and T. Matsue, *Angew. Chem., Int. Ed.*, 2012, **51**, 6648–6652.
25 K. Ino, W. Saito, M. Koide, T. Umemura, H. Shiku and T. Matsue, *Lab Chip*, 2011, **11**, 385–388.
26 K. Ino, Y. Kanno, T. Nishijo, T. Goto, T. Arai, Y. Takahashi, H. Shiku and T. Matsue, *Chem. Commun.*, 2012, **48**, 8505–8507.
27 M. Sen, K. Ino, H. Shiku and T. Matsue, *Lab Chip*, 2012, **12**, 4328–4335.
28 K. Ino, T. Goto, Y. Kanno, K. Y. Inoue, Y. Takahashi, H. Shiku and T. Matsue, *Lab Chip*, 2014, **14**, 787–794.
29 K. Ino, T. Nishijo, Y. Kanno, F. Ozawa, T. Arai, Y. Takahashi, H. Shiku and T. Matsue, *Electrochemistry*, 2013, **81**, 682–687.
30 K. Ino, T. Nishijo, Y. Kanno, H. Shiku and T. Matsue, *ECS Trans.*, 2013, **50**, 205–210.
31 K. Ino, Y. Kanno, T. Nishijo, H. Komaki, Y. Yamada, S. Yoshida, Y. Takahashi, H. Shiku and T. Matsue, *Anal. Chem.*, 2014, **86**, 4016–4023.
32 O. Niwa, Y. Xu, H. B. Halsall and W. R. Heineman, *Anal. Chem.*, 1993, **65**, 1559–1563.
33 O. Niwa, M. Morita and H. Tabei, *Anal. Chem.*, 1990, **62**, 447–452.
34 Y. Kanno, T. Goto, K. Ino, K. Y. Inoue, Y. Takahashi, H. Shiku and T. Matsue, *Anal. Sci.*, 2014, **30**, 305–309.
35 Y. Kanno, K. Ino, K. Y. Inoue, M. Sen, A. Suda, R. Kunikata, M. Matsudaira, H. Abe, C.-Z. Li, H. Shiku and T. Matsue, *J. Electroanal. Chem.*, 2015, **741**, 109–113.
36 C. Cannes, F. Kanoufi and A. J. Bard, *J. Electroanal. Chem.*, 2003, **547**, 83–91.
37 A. Harper and M. R. Anderson, *Sensors*, 2010, **10**, 8248–8274.
38 H. Kurosawa, T. Imamura, M. Koike, K. Sasaki and Y. Amano, *J. Biosci. Bioeng.*, 2003, **96**, 409–411.
39 M. Foquet, J. Korlach, W. Zipfel, W. W. Webb and H. G. Craighead, *Anal. Chem.*, 2002, **74**, 1415–1422.
40 R. Obregon, Y. Horiguchi, T. Arai, S. Abe, Y. Zhou, R. Takahashi, A. Hisada, K. Ino, H. Shiku and T. Matsue, *Talanta*, 2012, **94**, 30–35.
41 W. Dauer and S. Przedborski, *Neuron*, 2003, **39**, 889–909.
42 H. A. Pohl, *J. Appl. Phys.*, 1951, **22**, 869–871.
43 T. Yasukawa, H. Hatanaka and F. Mizutani, *Anal. Chem.*, 2012, **84**, 8830–8836.
44 J. Ramon-Azcon, S. Ahadian, M. Estili, X. Liang, S. Ostrovidov, H. Kaji, H. Shiku, M. Ramalingam, K. Nakajima, Y. Sakka, A. Khademhosseini and T. Matsue, *Adv. Mater.*, 2013, **25**, 4028–4034.
45 D. R. Albrecht, R. L. Sah and S. N. Bhatia, *Biophys. J.*, 2004, **87**, 2131–2147.
46 D. R. Albrecht, G. H. Underhill, T. B. Wassermann, R. L. Sah and S. N. Bhatia, *Nat. Methods*, 2006, **3**, 369–375.
47 L. J. Yang, P. P. Banada, M. R. Chatni, K. S. Lim, A. K. Bhunia, M. Ladisch and R. Bashir, *Lab Chip*, 2006, **6**, 896–905.
48 C.-T. Ho, R.-Z. Lin, W.-Y. Chang, H.-Y. Chang and C.-H. Liu, *Lab Chip*, 2006, **6**, 724–734.
49 I. Doh and Y. H. Cho, *Sens. Actuators, A*, 2005, **121**, 59–65.
50 N. Mittal, A. Rosenthal and J. Voldman, *Lab Chip*, 2007, **7**, 1146–1153.
51 N. Matsumoto, T. Matsue and I. Uchida, *Bioelectrochem. Bioenerg.*, 1994, **34**, 199–202.
52 T. Murata, T. Yasukawa, H. Shiku and T. Matsue, *Biosens. Bioelectron.*, 2009, **25**, 913–919.
53 P. Bajaj, D. Marchwiany, C. Duarte and R. Bashir, *Adv. Healthcare Mater.*, 2013, **2**, 450–458.

